



## Research Paper

## Improving sediment discharge efficiency in drip emitters via Tesla-inspired microchannels: PyFluent simulation and SHAP-based structural insights

Peng Hou<sup>a</sup>, Tuo Yin<sup>b</sup>, Shengqi Jian<sup>a</sup>, Yan Li<sup>c</sup>, Xinhao Gao<sup>c</sup>, Xueli Zhang<sup>a</sup>, Changjian Ma<sup>c,d,\*</sup><sup>a</sup> School of Water Conservancy and Transportation, Zhengzhou University, Zhengzhou, 450001, China<sup>b</sup> College of Water Resources and Civil Engineering, China Agricultural University, Beijing, 100083, China<sup>c</sup> State Key Laboratory of Nutrient Use and Management, Institute of Agricultural Resources and Environment, Shandong Academy of Agricultural Sciences, Jinan, 250100, China<sup>d</sup> National Center of Technology Innovation for Comprehensive Utilization of Saline-Alkali Land, Institute of Modern Agriculture on Yellow River Delta of SAAS, Dongying, 257091, China

## ARTICLE INFO

## Keywords:

Micro-scale water-sediment coupled flow  
Particle transport dynamics  
Emitter structural optimisation  
Two-phase flow simulation

## ABSTRACT

Sediment deposition is a critical factor contributing to emitter clogging and flow instability in drip irrigation systems, particularly under sediment-laden water conditions. At the micro-scale (10–1000 µm), flow and particle transport within emitter channels are governed by complex interactions involving confinement effects, turbulent structures, and particle-wall interactions. However, the mechanisms controlling sediment migration and removal remain insufficiently understood, and there is a lack of robust modelling tools to support emitter design under such conditions. In this study, a novel Tesla-inspired bidirectional microchannel was proposed to improve hydraulic performance and sediment discharge efficiency. A high-resolution Euler–Lagrange two-phase flow model was developed using PyFluent, integrating key physical processes including Schiller–Naumann drag, Saffman lift, turbulent dispersion, and rebound boundary conditions to simulate sediment behaviour at particle scale. Simulation results revealed that the inclusion of reverse-flow units significantly enhanced shear zones and vortex intensity, leading to a 97.18 % increase in turbulent kinetic energy (TKE, CFD simulation). Under different forward- and reverse-flow unit configurations, PSD and QSDV both decreased by 22.73 %–53.40 %. Variations under different channel widths and depths showed different ranges due to QSDV being normalised by volume (all CFD simulation results). Contribution analysis using SHapley Additive exPlanations (SHAP) identified hydraulic diameter and the number of forward-flow units as dominant structural factors influencing sediment transport through their effects on local energy dissipation and flow field reorganisation. These findings provide a physically interpretable and practically applicable modelling framework for optimising emitter design. This study proposed approach offers new insights into the coupling between microchannel geometry and sediment dynamics, supporting the development of anti-clogging strategies in drip irrigation systems using non-conventional water sources.

## 1. Introduction

Agricultural irrigation pipeline systems are fundamental to ensuring global food security, particularly under the growing pressure of freshwater scarcity. In recent years, irrigation technologies have shifted toward enhanced water use efficiency and precision (Zhang et al., 2021). Drip irrigation, as one of the most efficient irrigation methods, has been widely promoted for its potential to reduce water consumption while maintaining crop productivity (Zhang et al., 2021). In water-limited

regions such as Northwest China, Southwestern Europe, and Southeastern Africa, the use of sediment-laden surface water has become a practical solution for sustaining irrigated agriculture (Hou, Puig-Bargués, et al., 2024; Puertes et al., 2021).

However, long-term operation of drip systems with high-sediment water sources poses technical challenges, particularly emitter clogging due to sediment accumulation within microchannels. This results in reduced flow uniformity and diminished system performance (Xu et al., 2020; Yang, Wang, et al., 2024; Zhou et al., 2019). Existing mitigation

\* Corresponding author. State Key Laboratory of Nutrient Use and Management, Institute of Agricultural Resources and Environment, Shandong Academy of Agricultural Sciences, Jinan, 250100, China.

E-mail address: [saafitigation@163.com](mailto:saaftigation@163.com) (C. Ma).

strategies such as external filtration systems (Hua et al., 2016; Shen et al., 2022) and chemical flushing agents (Shrestha et al., 2020; Zhang et al., 2022)—can be effective but are often cost-intensive or unsuitable for low-input agricultural systems (Song et al., 2019). Recent studies have shown that emitters themselves may exhibit self-cleaning potential under certain hydraulic conditions, particularly for fine sediment particles (Hou, Puig-Bargués, et al., 2024; Hou, Liu, et al., 2024). Their clogging process has been reported to be primarily governed by parameters such as the average cross-sectional velocity, the width-to-depth ratio, and the relative hydraulic radius (Li et al., 2019, 2024). Furthermore, it has been suggested that enhancing near-wall shear stress, mean flow velocity, and turbulent kinetic energy can effectively improve the removal efficiency of sediment and other particulate matter (AL-Muhammad et al., 2018; Dallagi et al., 2024; De Marchis et al., 2025). While promising, these designs require a clear understanding of the flow–particle interaction mechanisms to ensure reliable performance under different sediment and hydraulic conditions.

Emitter channels typically range from 10 to 1000 µm in characteristic dimension, placing them in the microfluidic regime (Kovalchuk and Simmons, 2023). At this scale, two-phase water–sediment flow is governed by nonlinear fluid–particle interactions, wall-induced effects, shear-driven disturbances, and vortex structures (Shi et al., 2019). The influence of particle feedback on the flow field and the spatial heterogeneity caused by broad particle size distributions further complicate the system dynamics (Cha et al., 2022). These features challenge the applicability of conventional macro-scale modelling approaches.

Over the past decades, geometric optimisation of emitter microchannels has predominantly centred on labyrinth, zigzag, and fractal configurations (Li et al., 2019). While each offers certain anti-clogging benefits, these designs largely depend on steady, unidirectional flow paths and seldom exploit active flow reversal or vortex trapping as mechanisms for sediment resuspension (De Marchis et al., 2025; Feng et al., 2018). In contrast, the Tesla-inspired microchannel approach offers a distinct physical mechanism: by employing asymmetrical expansion–contraction geometries, it generates preferential flow directions, induces localised recirculation zones, and enhances shear gradients, thereby facilitating particle detachment and mitigating long-term sediment deposition (Liu et al., 2022). Unlike labyrinth, zigzag, or fractal channels, the Tesla-type configuration integrates forward- and reverse-flow disturbance units in series, enabling self-cleaning through alternating flow regimes while maintaining discharge stability. This principle has been successfully applied in other microfluidic devices for particle separation and debris removal, but its targeted adaptation for drip emitter anti-clogging remains underexplored.

While computational fluid dynamics (CFD) has been employed to simulate internal flow behaviour in emitters (Feng et al., 2018; Li et al., 2023; Tong et al., 2025; Wu et al., 2013), most efforts have focused on single-phase hydraulics. Studies addressing fully coupled water–sediment dynamics under micro-scale conditions remain limited. Although CFD–DEM models have been used in devices such as hydrocyclones and separators (Song et al., 2017; Wang and Wu, 2018), their application in emitter microchannels is restricted by modelling complexity and resolution limitations (Liu et al., 2023; Zhou et al., 2020, 2021). Therefore, there is a need to develop high-resolution, interpretable, and application-oriented modelling tools to support emitter design under sediment-laden conditions.

To address this gap, this study proposes a Tesla-inspired bidirectional microchannel design that enhances flow structuring and sediment removal capacity. A high-fidelity Euler–Lagrange two-phase flow model was established using PyFluent to simulate sediment migration within the microchannel. SHAP (Shapley Additive Explanations) was employed to evaluate the contribution of structural parameters to hydraulic and anti-clogging performance. Specifically, this study aims to (1) construct a high-resolution numerical framework for sediment transport analysis in emitters, (2) explore the influence pathways of structural variables on flow and sediment behaviour, and (3) provide an optimised emitter

design strategy for improving hydraulic and sediment discharge performance. Although the experiments and simulations are based on sediment characteristics and hydraulic conditions typical of the Yellow River basin, the underlying mechanisms and design principles are applicable to other sediment-laden irrigation contexts worldwide—particularly in regions where surface water contains fine to medium suspended particles, such as parts of South Asia, the Middle East, and North Africa. Thus, the approach offers both site-specific relevance and broader generalisability for anti-clogging emitter design. The results provide theoretical support for the design of robust drip irrigation systems capable of long-term operation under sediment-laden water conditions, and advance the understanding of micro-scale two-phase flow in agricultural water management.

## 2. Materials and methods

### 2.1. Experimental setup and operation of the sediment-laden drip irrigation system

This study was conducted at the Dengkou Irrigation Experimental Station, located in the Hetao Irrigation District of Bayannur, Inner Mongolia, China. The experiment aimed to simulate the operational conditions of drip irrigation systems under high sediment load scenarios. The sediment-laden irrigation water was prepared using native Yellow River sediment, with particle sizes ranging from 0 to 100 µm and a sediment concentration of 1 g/L, replicating the typical sediment characteristics of the Yellow River diversion environment. The experimental drip irrigation system consisted of three primary components: a water storage unit, a two-stage filtration system, and a dripline equipped with emitters. The filtration unit employed a combination of gravel filtration (with uniform media size of 1–2 mm) and a 120-mesh disc filter, effectively removing large particles and suspended flocs from the source water. The total length of the dripline was 18 m, along which four types of flat emitters were installed, labelled as E1, E2, E3, and E4. Emitters E1 and E2 featured serrated flow path structures, whereas E3 and E4 adopted fractal flow path configurations. The key structural parameters of the four emitters are summarised in Table 1, and the corresponding schematic diagrams of the internal flow path structures are presented in Fig. 1.

**Emitter flow rate measurement:** emitter outflow was measured using the gravimetric method, following the procedure described by Xiao et al. (2021). Given that ambient temperature fluctuations in the outdoor environment could influence water viscosity and thus affect flow rate measurements, temperature correction was applied to the raw data using the empirical correction formula proposed by Xiao et al. (2021), to improve measurement accuracy and consistency.

**Sediment deposition and discharge ratio measurement:** the sediment discharge performance was evaluated via a sampling and weighing method. Water samples were collected using 300 mL sampling bottles at both the system inlet and the emitter outlet. After drying, the difference in sediment dry mass was determined and used to calculate the emitter's sediment discharge ratio. The testing protocol followed the method outlined by Hou, Puig-Bargués, et al. (2024). The calculation formula for the sediment deposition and discharge ratio  $\phi$  is shown in Equation (1):

**Table 1**  
Characteristic structural parameters of the emitters.

| Emitter type | Flow rate (L/h) | Emitter structural parameters |            |            | Wall thickness (mm) | Origin |
|--------------|-----------------|-------------------------------|------------|------------|---------------------|--------|
|              |                 | length (mm)                   | width (mm) | depth (mm) |                     |        |
| E1           | 1.0             | 47.13                         | 0.91       | 1.21       | 0.2                 | China  |
| E2           | 1.6             | 35.52                         | 0.89       | 0.64       | 0.2                 | China  |
| E3           | 1.0             | 22.83                         | 0.82       | 0.58       | 0.2                 | China  |
| E4           | 1.6             | 40.36                         | 0.72       | 0.72       | 0.2                 | China  |

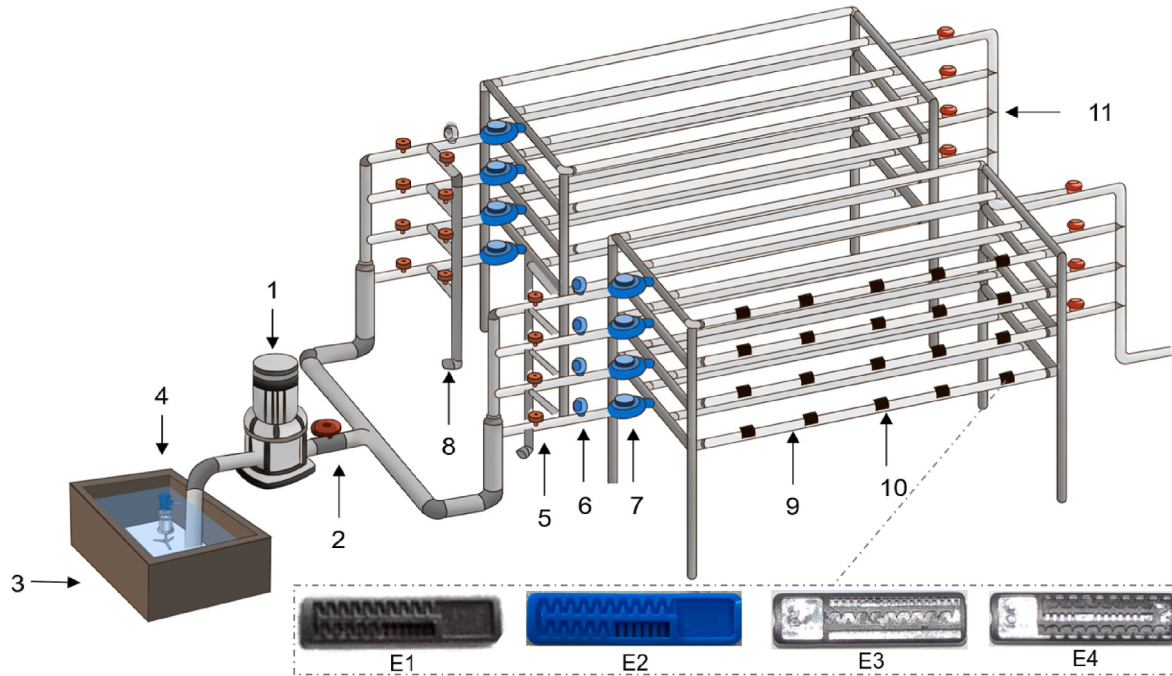


**Fig. 1.** Schematic diagram of the experimental setup. 1. Water pump; 2. Butterfly valve; 3. Water tank; 4. Stirrer; 5. Small lamination filter; 6. Pressure gauge; 7. Water metre; 8. Return pipe; 9. Drip irrigation tape (pipe); 10. Emitter; 11. Flushing device.

$$\varphi = \frac{\sum_{i=1}^n m_i \times n_i \times 15}{\sum_{i=1}^n \rho_i \times v_i} \times 100\% \quad (1)$$

where,  $m_i$  is the average dry weight of clogging substances in emitter during the  $i$ -th flow measurement (each 15 m long),  $\text{g m}^{-1}$ ;  $n_i$ , the corresponding number of emitter (each 15 m long drip irrigation), count;  $\rho_i$ , the  $i$ -th emitter outflow sand concentration,  $\text{g L}^{-1}$ ; and  $v_i$ , the cumulative irrigation water volume, L.

## 2.2. Numerical simulation method

### 2.2.1. Governing equations

Numerical simulations of the internal water–sediment two-phase flow in the emitter were conducted using PyFluent (2022.R2) as the computational platform. The water phase was treated as the continuous phase and solved within the Eulerian framework using steady-state three-dimensional Reynolds-averaged Navier–Stokes (RANS) equations, including the continuity equation and momentum equations. The continuous phase was modelled using the RNG k– $\epsilon$  turbulence model, selected for its numerical stability and adaptability in flows with strong vortex structures, curvature, and rotation (Feng et al., 2018; Li et al., 2023). Compared to the standard k– $\epsilon$  model, the RNG formulation offers improved resolution of local turbulence features, making it suitable for the highly curved, heterogeneous flow fields of emitter channels (Sun et al., 2021). While agreement with experiments was good, the RNG k– $\epsilon$  model may be less accurate in low-Reynolds-number regimes; future work could evaluate alternative closures such as the k– $\omega$  SST model to improve near-wall turbulence resolution.

Sediment particle motion was resolved using a three-dimensional steady-state Euler–Lagrange approach. The continuous phase was solved with the Eulerian Navier–Stokes equations, while sediment particles were tracked using a Lagrangian-based Discrete Phase Model (DPM) (Khaldi et al., 2016), enabling detailed trajectory and force analysis (Ching et al., 2020; Yang, Xi, et al., 2024). The dominant forces considered included gravity and buoyancy for settling behaviour; drag force via the Schiller–Naumann correlation for low-to-moderate

Reynolds numbers (Pietrzyk et al., 2022); Saffman lift force for transverse migration in strong shear zones (Abdorahimzadeh et al., 2024); and turbulent dispersion to avoid underestimating fine particle transport (Boutsikakis et al., 2022). The physical properties of the water phase were set as a density of  $998.2 \text{ kg m}^{-3}$  and a dynamic viscosity of  $0.001 \text{ kg (m·s)}^{-1}$ . The particles were represented as calcium carbonate with a density of  $2800 \text{ kg m}^{-3}$ . The governing equation for particle motion is expressed as Equation (2):

$$m_p \frac{dv_p}{dt} = F_{g,b} + F_D + F_L + F_{turb} \quad (2)$$

Where,  $m_p$  is particle mass;  $v_p$  is particle vector;  $t$  is time;  $F_{g,b}$  is combined force (gravity-buoyancy);  $F_D$  is drag force;  $F_L$  is saffman lift force;  $F_{turb}$  is turbulent dispersion

#### (1) Combined force (Gravity and Buoyancy)

Due to the significantly higher density of sediment particles compared to water, gravitational settling effects—including both gravity and buoyancy—were considered in the particle force balance. The corresponding formulations are presented in Equations (3)–(5).

$$F_g = m_p g = \frac{\pi}{6} d_p^3 \rho_p g \quad (3)$$

$$F_b = -\frac{\pi}{6} d_p^3 \rho_f g \quad (4)$$

$$F_{g,b} = \frac{\pi}{6} d_p^3 (\rho_p - \rho_f) g \quad (5)$$

where,  $\rho_p$  is particle density;  $d_p$  is particle diameter;  $\rho_f$  is fluid density;  $g$  is gravitational acceleration;  $F_g$  is gravity;  $F_b$  is buoyancy;  $F_{g,b}$  is combined force (gravity-buoyancy)

#### (2) Drag force

The flow velocity within the emitter channels is typically high, resulting in significant drag forces acting on the sediment particles.

Therefore, drag force was explicitly considered in the simulation.

$$\mathbf{F}_D = \frac{18\mu}{\rho_p d_p^2} C_D Re_p (\mathbf{v}_f - \mathbf{v}_p) \quad (6)$$

where,  $\mu$  is fluid dynamic viscosity;  $C_D$  is drag coefficient;  $Re_p$  is particle Reynolds number;  $\mathbf{v}_f$  is fluid vector;  $\mathbf{v}_p$  is particle vector;

$C_D$  is calculated according to the formulations given in Equations (7) and (8).

$$C_D = \frac{24}{Re_p} \left( 1 + 0.15 Re_p^{0.687} \right) \quad (7)$$

$$Re_p = \frac{\rho_f d_p |\mathbf{v}_f - \mathbf{v}_p|}{\mu} \quad (8)$$

where,  $\rho_f$  is fluid density;

### (3) Saffman lift force

Shear-dominated flow structures may exist within the emitter, such as those arising in contraction-expansion zones, secondary flows, and vortex regions. In such conditions, lift force can significantly influence the trajectories of sediment particles. The lift force is calculated according to Equation (9).

$$\mathbf{F}_L = C_L \rho_f \nu^{0.5} |\mathbf{v}_f - \mathbf{v}_p| (\boldsymbol{\omega} \times (\mathbf{v}_f - \mathbf{v}_p)) \quad (9)$$

where,  $C_L$  is lift coefficient;  $\nu$  is kinematic viscosity;  $\boldsymbol{\omega}$  is fluid vorticity vector.

### (4) Turbulent dispersion

The internal flow within the emitter is typically turbulent. The presence of stochastic turbulent fluctuations affects the dispersion of fine particles, causing them to distribute randomly within the flow domain. Therefore, the effect of turbulent dispersion was taken into account, and its formulation is given as follows:

$$\mathbf{F}_{turb} = \xi \sqrt{\frac{2}{3}} k \quad (10)$$

where,  $k$  is turbulent kinetic energy(unit:  $\text{m}^2 \text{s}^{-2}$ );  $\xi$  is random variable.

### 2.2.2. Boundary conditions

In the numerical model, a pressure inlet boundary condition was applied at the inlet with a fixed pressure of 0.10 MPa, while the outlet was defined as a pressure outlet with a pressure of 0 MPa. All remaining walls were assigned rebound-type collision boundary conditions, with the normal restitution coefficient set to 0.30 and the tangential restitution coefficient set to 0.50, to account for momentum changes during particle-wall interactions (Guo et al., 2021). Sediment particles in the Discrete Phase Model were injected from the pressure inlet surface of the emitter geometry. The injection was defined using a concentration-controlled approach based on the measured sediment concentration of 1 g/L, corresponding to a mass loading ratio of  $1.0 \times 10^{-6}$ . According to De Marchis and Milici (2016), two-way coupling becomes important when the mass loading ratio exceeds  $1.0 \times 10^{-6}$ , therefore, a one-way coupling approach was adopted, in which the fluid phase influences particle motion while particle-fluid momentum exchange is neglected. This assumption is consistent with the expected minimal feedback effect under the present experimental conditions. The number of particle streams was set to ensure statistical convergence of particle trajectories without imposing excessive computational cost, and the total particle mass flow rate was matched to that of the continuous water phase at the inlet to maintain the target sediment concentration.

The particle size distribution was fitted based on field-measured sediment samples from the Yellow River. Given that the Yellow River

sediment at the study site is dominated by fine particles with nearly spherical geometry and low concentration, particles in the Discrete Phase Model were assumed to be spherical. This simplification was adopted because shape effects are expected to be minimal under these conditions, although we acknowledge that particle morphology, surface roughness, and adhesive properties can influence clogging behaviour. The measured median particle diameter was 61.35  $\mu\text{m}$ , and the corresponding particle size distribution curve is provided in the Supplementary Material (Fig. S1). A Rosin-Rammler distribution function was used to represent the mixed particle size spectrum, with a spread parameter of 1.30. The fitted function is expressed in Equation (11). For numerical solving, the SIMPLEC algorithm was employed to couple pressure and velocity fields. Second-order upwind schemes were applied for spatial discretisation, and the convergence criterion for all residuals was set to  $10^{-4}$  to ensure both computational accuracy and numerical stability.

$$R(d) = 1 - e^{-\left(\frac{d}{d_m}\right)^n} \quad (11)$$

where,  $R(d)$  is the cumulative distribution function representing the fraction of particles with diameters smaller than a given size  $d$ ,  $d_m$  is the mean particle diameter,  $n$  is the spread parameter.

### 2.2.3. Geometry modelling and mesh generation

The three-dimensional geometry of the emitter was constructed using NX UG software. Pre-processing and mesh generation were conducted in ICEM CFD. To ensure accurate resolution of the complex internal structures, an unstructured mesh was adopted, with a global element size of 0.02 mm. The mesh quality was validated through a mesh independence test, confirming an appropriate balance between numerical accuracy and computational efficiency.

### 2.3. Emitter flow path configuration and design parameters

Based on the conventional Tesla-type flow path (Fig. 2a), this study proposes a novel bidirectional disturbance configuration that integrates both forward and reverse units. This design introduces strong flow collision between the main flow zone and the reverse-disturbance region, leading to significant redistribution of flow energy and the formation of pronounced geometric directionality (Fig. 2b). The contrasting flow directions result in complex response mechanisms in both hydraulic and sediment transport performance, making the distribution of forward and reverse units a critical structural design parameter. Preliminary experiments revealed that when the total number of flow units is fewer than nine, the emitter fails to maintain stable dripping and instead produces intermittent jetting. To ensure operational stability, the total number of flow units was fixed at nine in this study. The number of forward-flow units was varied from 0 to 9, with the corresponding number of reverse-flow units adjusted from 9 to 0, generating a series of structural combinations. To comprehensively evaluate the influence of geometric parameters on two-phase flow behaviour, four flow path widths (0.25 mm, 0.40 mm, 0.55 mm, and 0.70 mm) and four depths (0.25 mm, 0.40 mm, 0.55 mm, and 0.70 mm) were considered, resulting in 160 structural configurations in total, the experimental treatments are shown in Table 2, with full details provided in Supplementary Table S1. The spatial layout and parameter combinations for all designs are illustrated in Fig. 2c and were used for subsequent simulations and performance response analyses.

### 2.4. Fuzzy comprehensive evaluation method

In this study, a fuzzy comprehensive evaluation method was employed to assess the 160 treatments, primarily considering their hydraulic performance (flow index, flow coefficient) and anti-clogging performance (quantity of sediment deposited per unit volume, percentage of sediment deposition). A comprehensive weighting system

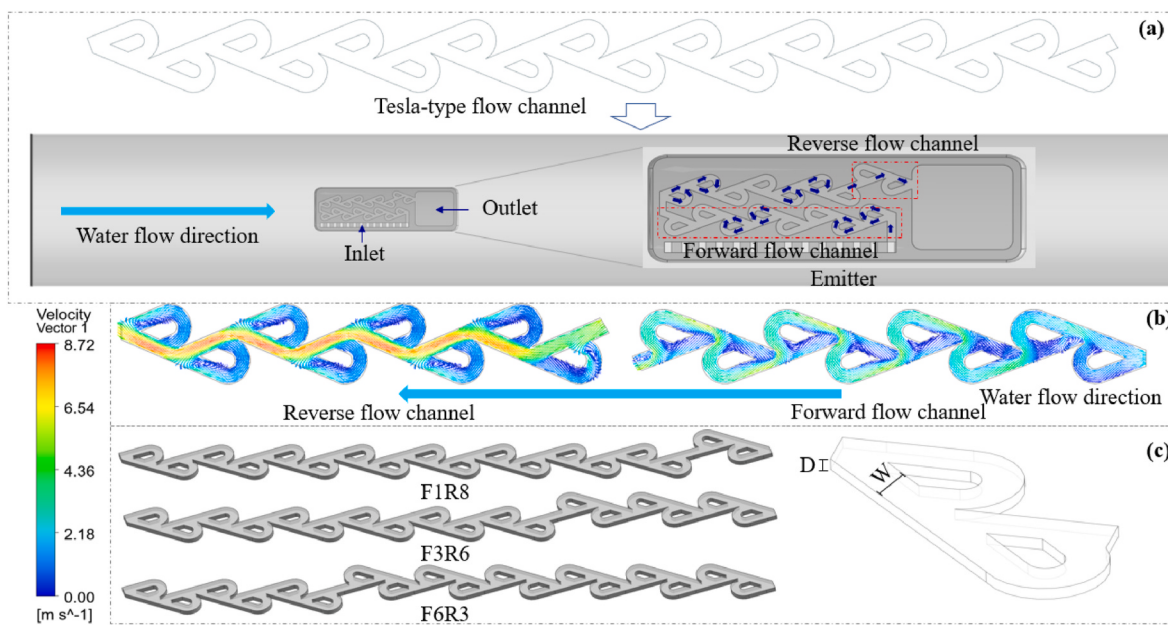


**Fig. 2.** Structural optimisation of the novel flow path design. (a) Schematic of the novel emitter with a Tesla-type bidirectional flow path; (b) Comparison of flow characteristics in forward and reverse units; (c) Structural parameter settings of the microchannel, including width, depth, and unit configuration.

**Table 2**  
Experimental design.

| Treatment ID | Forward Units | Reverse Units | Width (mm)              | Depth (mm)              |
|--------------|---------------|---------------|-------------------------|-------------------------|
| 1–16         | 0             | 9             | 0.25/0.40/<br>0.55/0.70 | 0.25/0.40/<br>0.55/0.70 |
| 17–32        | 1             | 8             | 0.25/0.40/<br>0.55/0.70 | 0.25/0.40/<br>0.55/0.70 |
| 33–48        | 2             | 7             | 0.25/0.40/<br>0.55/0.70 | 0.25/0.40/<br>0.55/0.70 |
| 49–64        | 3             | 6             | 0.25/0.40/<br>0.55/0.70 | 0.25/0.40/<br>0.55/0.70 |
| 65–80        | 4             | 5             | 0.25/0.40/<br>0.55/0.70 | 0.25/0.40/<br>0.55/0.70 |
| 81–96        | 5             | 4             | 0.25/0.40/<br>0.55/0.70 | 0.25/0.40/<br>0.55/0.70 |
| 97–112       | 6             | 3             | 0.25/0.40/<br>0.55/0.70 | 0.25/0.40/<br>0.55/0.70 |
| 113–128      | 7             | 2             | 0.25/0.40/<br>0.55/0.70 | 0.25/0.40/<br>0.55/0.70 |
| 129–144      | 8             | 1             | 0.25/0.40/<br>0.55/0.70 | 0.25/0.40/<br>0.55/0.70 |
| 145–160      | 9             | 0             | 0.25/0.40/<br>0.55/0.70 | 0.25/0.40/<br>0.55/0.70 |

was established, with the following weights assigned: flow index ( $\gamma$ ), 0.25; flow coefficient (K), 0.25; quantity of sediment deposited per unit volume (QSDV), 0.25; and percentage of sediment deposition (PSD), 0.25. Based on these indicators and their weights, a fuzzy comprehensive evaluation set and factor set were constructed, and the evaluation matrix and membership functions were determined. The detailed calculation process is provided in the Supplementary Materials.

## 2.5. Data analysis

To quantitatively assess the relative influence of emitter structural parameters on hydraulic performance and sediment discharge capacity, this study employed SHAP (SHapley Additive exPlanations) for interpretable analysis of the simulation results. SHAP is a game-theory-based global feature attribution method that enables the decomposition of model predictions into the marginal contributions of each input variable while maintaining high model accuracy (Felix et al., 2025; Hancock

et al., 2025; Yang, Guan, et al., 2024). In this study, a simulation dataset was constructed based on different combinations of structural parameters, including the number of forward/reverse flow units, channel width and depth, hydraulic diameter, and width-to-depth (W/D) ratio. Gradient boosting decision trees (XGBoost, tree depth = 31, learning rate = 0.1, number of CVs = 3) were trained to predict key performance indicators, including the flow index ( $\gamma$ ), flow coefficient (K), and sediment discharge metrics such as the percentage of sediment deposition (PSD) and the quantity of sediment deposited per unit volume (QSDV). To assess feature importance in the model dataset, Shapley Additive Explanations (SHAP) values were computed for each observation using the final model, followed by marginal effect analysis of individual variables. The absolute SHAP values quantify variable contribution magnitudes. Mean absolute SHAP values were subsequently derived per variable for comparative importance evaluation, implemented through Python's shap package. Once high model accuracy was achieved ( $R^2 > 0.95$ ), SHAP values were computed for the trained regression models to quantify the relative contribution of each input parameter to the performance outcomes ( $R^2 = 0.89$ , MAE = 0.06, RMSE = 0.08). This analysis enabled the identification of dominant design variables and provided a physically interpretable link between flow path structure and system performance.

## 3. Results

### 3.1. Validation of the numerical model

To evaluate the accuracy of the proposed water-sediment two-phase flow model, numerical simulations were performed on four types of flat emitters using the PyFluent platform. Simulated results for both emitter outflow rate and sediment deposition and discharge ratio were compared against experimental measurements. The validation results are presented in Fig. 3. As shown in Fig. 3a, the simulated flow rates were slightly lower than the measured values; however, the relative errors were within the range of 3.68 %–6.86 %, indicating that the model provides satisfactory accuracy in predicting emitter hydraulic performance. Fig. 3b presents the comparison for the sediment deposition and discharge ratio. The simulated values exhibited a minor underestimation relative to the experimental data, with deviations ranging from 4.69 % to 10.59 %, which are still considered acceptable. Overall,

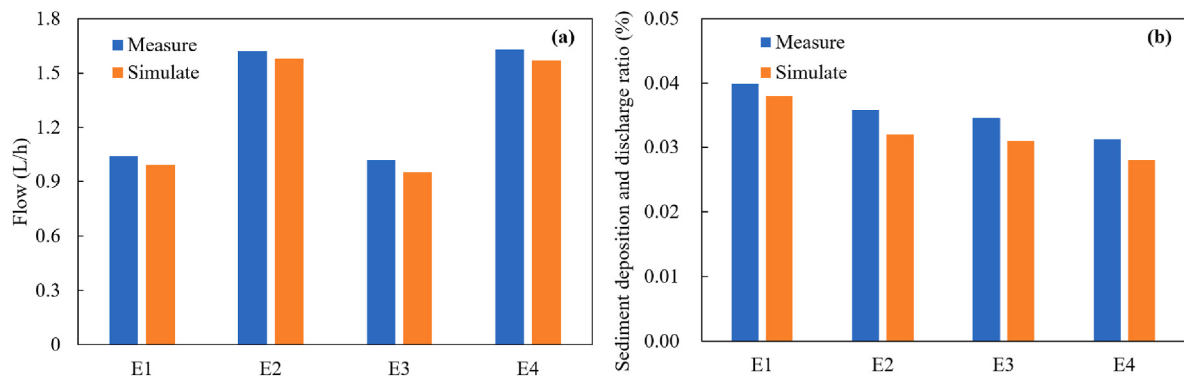


**Fig. 3.** Validation of the numerical simulation model. (a) Comparison between simulated and measured emitter flow rates; (b) Comparison between simulated and measured sediment deposition and discharge ratios.

the PyFluent-based two-phase flow model developed in this study demonstrates high reliability in predicting both hydraulic behavior and sediment discharge performance of emitters. This provides a robust

foundation for the subsequent analysis of structural optimisation and performance improvement.

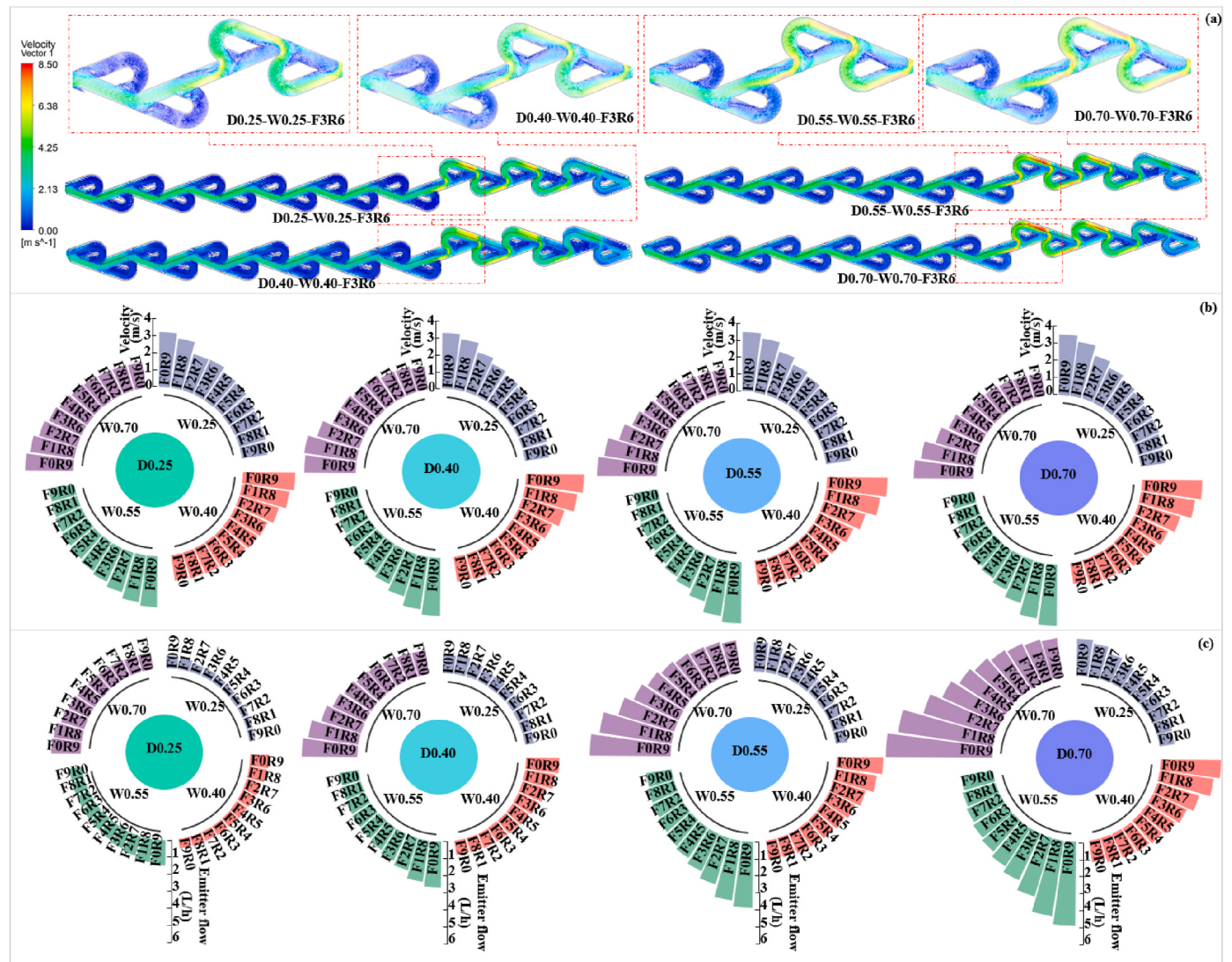


**Fig. 4.** Effects of structural parameters of the novel flow path configuration on emitter flow performance. (a) Internal velocity distribution for the F3R6 flow path configuration, illustrating localised high-velocity zones and flow uniformity patterns within the channel. (b) Variation in mean internal flow velocity across different structural parameter settings, reflecting changes in hydraulic efficiency. (c) Corresponding emitter flow rate under each configuration, demonstrating the overall impact of structural design on discharge capacity.

### 3.2. Effects of structural parameters on emitter flow rate under the novel flow path design

Under the proposed Tesla-inspired bidirectional flow path configuration, structural parameters exert a significant influence on the internal velocity distribution and outlet flow rate of the emitter. The simulation results are illustrated in Fig. 4. From the perspective of the ratio between forward and reverse units, a reduction in the number of forward-flow units led to a pronounced increase in both average internal velocity (Fig. 4b) and outlet flow rate (Fig. 4c). When comparing the two extreme configurations-F0R9 and F9R0, the F0R9 design exhibited an 87.23 %–165.87 % increase in average flow velocity and flow rate, respectively, under the constraint of a constant total unit number. Further analyses were conducted to explore the influence of geometric dimensions, specifically channel width and depth, on hydraulic performance. Taking the F3R6 configuration as an example (Fig. 4a), increasing the flow path width from 0.25 mm to 0.70 mm resulted in moderate fluctuations in average velocity, with changes ranging from –12.45 % to 15.17 %, while the outlet flow rate continuously increased by 145.11 %–203.79 %. Similarly, when the channel depth increased from 0.25 mm to 0.70 mm, the average velocity varied within a range of –14.07 %–27.45 %, accompanied by a corresponding flow rate enhancement of 140.61 %–256.87 %. These results highlight the nonlinear and dimensionally sensitive nature of flow responses in emitters under micro-scale geometric modifications.

### 3.3. Effects of structural parameters on hydraulic performance under the novel flow path design

The effects of different structural parameters on hydraulic performance under the proposed flow path configuration are illustrated in Fig. 5, including the flow index ( $\chi$ ) and flow coefficient (K). As shown, both  $\chi$  and K exhibited an increasing trend as the number of forward-flow units decreased and reverse-flow units increased. Compared with the F9R0 configuration, the F0R9 configuration yielded an enhancement of 23.23 %–44.83 % in the flow index and 150.39 %–246.57 % in the flow coefficient (Fig. 5a-h). For configurations with the same flow unit

distribution, increasing the channel width resulted in a fluctuating trend in the flow index but a consistent increase in the flow coefficient. When the width increased from 0.25 mm to 0.70 mm, the flow index varied within a range of –5.89 %–6.27 %, while the flow coefficient increased by 140.37 %–207.56 %. In contrast, increasing the channel depth from 0.25 mm to 0.70 mm led to a decreasing trend in the flow index (–0.75 % to –16.24 %), while the flow coefficient increased by 134.44 %–199.16 %. These results suggest that structural parameters exert distinct, and in some cases opposite, effects on the two hydraulic performance indicators, with flow coefficient being more responsive to geometric scaling than the flow index.

### 3.4. Effects of structural parameters on turbulence characteristics

The effects of different structural parameters under the novel flow path configuration on turbulence eddy dissipation and turbulent kinetic energy (TKE, unit:  $\text{m}^2 \text{ s}^{-2}$ ) are presented in Fig. 6. The three-dimensional spatial distributions of eddy dissipation and TKE are shown in Fig. 6a and b, respectively. As the number of forward-flow units decreased and the number of reverse-flow units increased, both turbulence eddy dissipation and TKE exhibited a notable increasing trend. Compared with the F9R0 configuration, the F0R9 design showed an increase of 35.31 %–113.74 % in eddy dissipation and 13.13 %–97.18 % in TKE, indicating that the introduction of reverse-flow structures effectively enhanced internal turbulence levels. For configurations with the same flow unit arrangement, increasing the channel width from 0.25 mm to 0.70 mm led to a decrease in both turbulence indices. Specifically, eddy dissipation and TKE decreased by 64.91 %–78.98 % and 12.54 %–56.31 %, respectively. This suggests that larger channel widths reduce shear gradients and local flow disturbances. In contrast, increasing the channel depth produced divergent effects: turbulence eddy dissipation exhibited a fluctuating trend, while TKE consistently increased. When the depth was increased from 0.25 mm to 0.70 mm, the change in eddy dissipation ranged from –24.06 % to 24.01 %, and TKE increased by 10.75 %–168.60 %. These findings demonstrate that flow channel depth plays a more significant role in regulating energy storage within the flow, whereas channel width more strongly affects energy

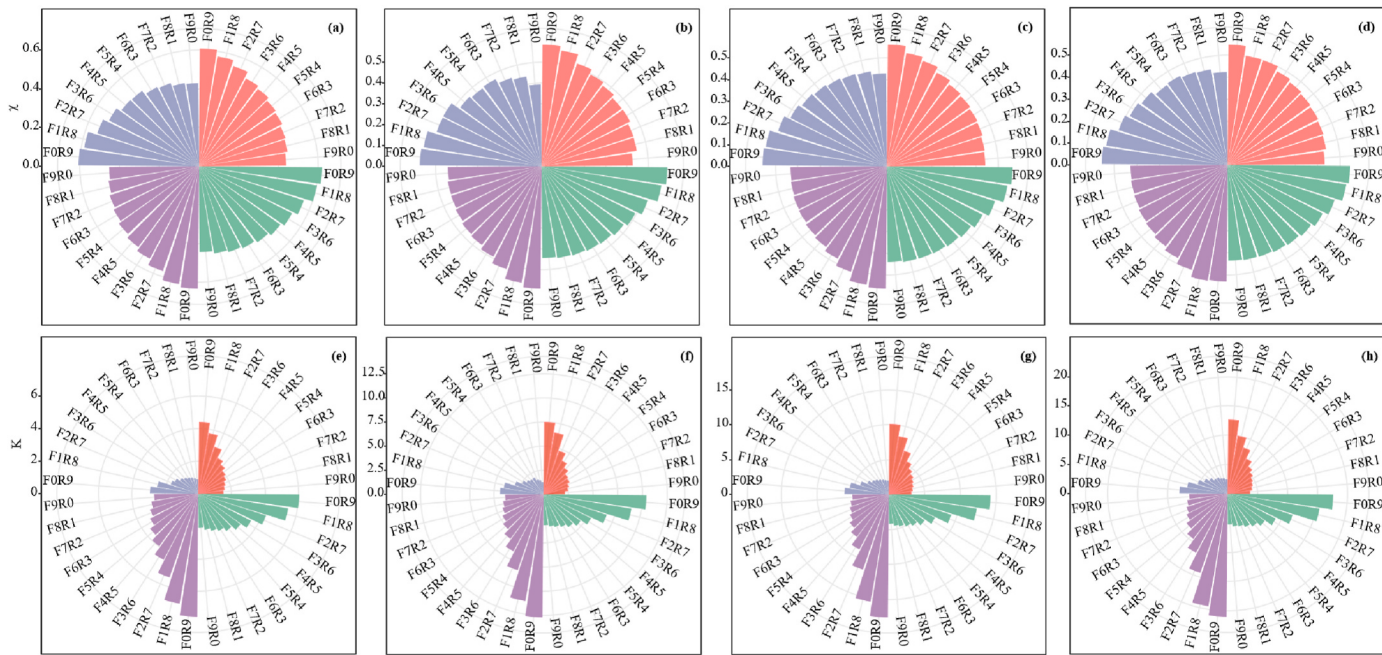


**Fig. 5.** Effects of structural parameters of the novel flow path configuration on hydraulic performance. (a) Flow index ( $\chi$ ) for different structural parameter combinations, indicating the degree to which discharge is sensitive to inlet pressure changes and reflecting hydraulic stability. (b) Flow coefficient (K) under varying configurations, representing the baseline discharge capacity at a reference pressure and showing how design modifications affect overall emitter output.

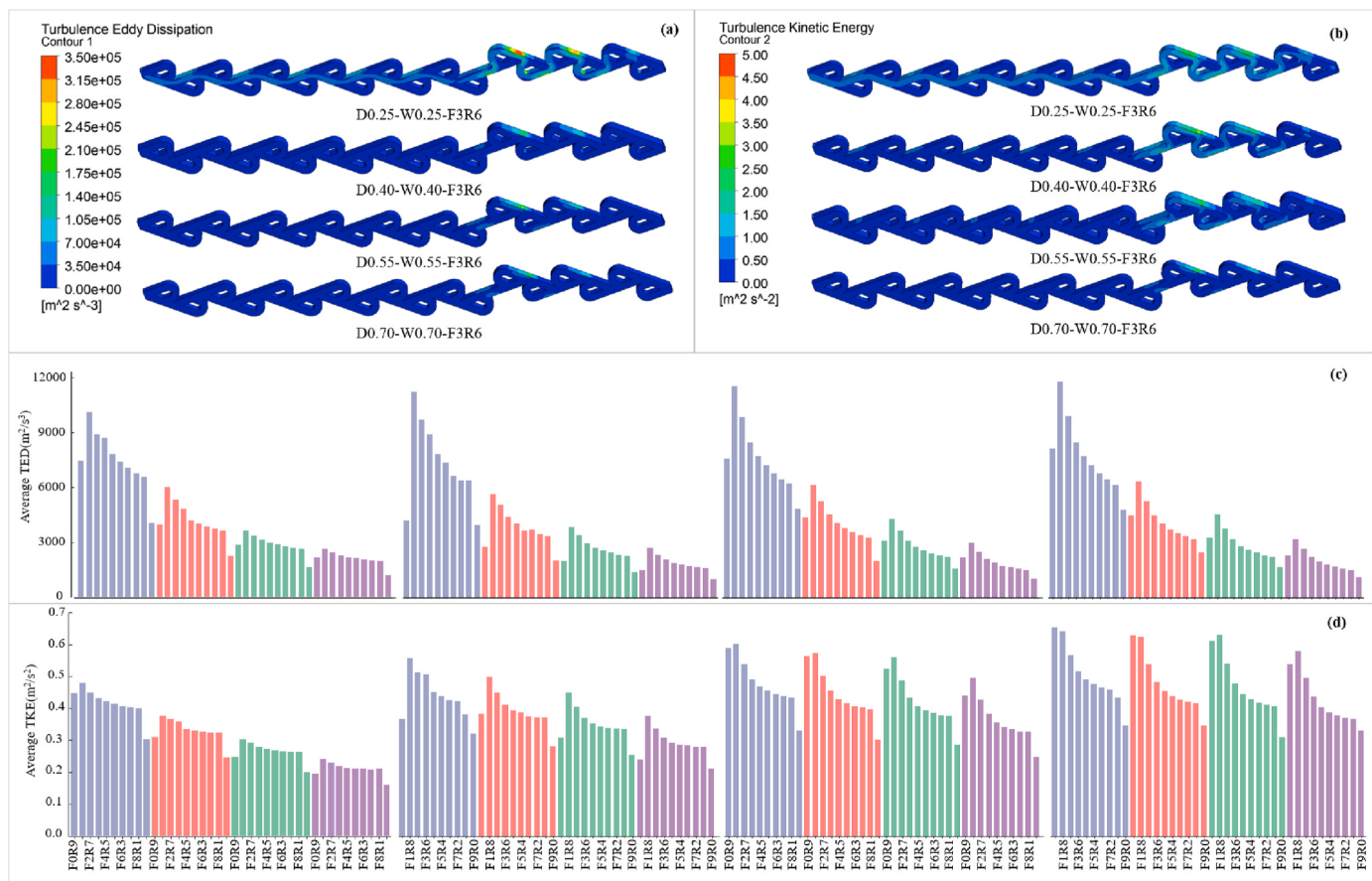


**Fig. 6.** Effects of structural parameters of the novel flow path configuration on turbulence characteristics. (a) Three-dimensional distribution of turbulence eddy dissipation within the emitter channel, showing localised high-dissipation zones where energy is rapidly converted into heat and smaller vortices. (b) Three-dimensional distribution of turbulence kinetic energy (TKE), highlighting regions of intense turbulent motion that influence sediment suspension and transport. (c) Average turbulence eddy dissipation for different structural configurations, reflecting the overall energy loss rate within the flow path. (d) Average turbulence kinetic energy, indicating the mean turbulent intensity and its dependence on structural design parameters, with implications for anti-clogging performance.

dissipation.

### 3.5. Effects of structural parameters on sediment discharge performance

The transport behaviour of sediment particles with different size classes under the F3R6 flow path configuration is shown in Fig. 7a. Particles with diameters of 0–41 µm were relatively evenly distributed within both the main flow and non-mainstream zones. As particle size increased, larger particles (41–100 µm) were primarily concentrated and transported within the main flow region, indicating a size-dependent migration pattern. Under various structural parameter settings of the novel flow path configuration, the percentage of sediment deposition (PSD) and the quantity of sediment deposited per unit volume (QSDV) were used to characterise sediment retention performance (Fig. 7b and c). Overall, as the number of forward-flow units decreased and reverse-flow units increased, both PSD and QSDV exhibited a clear downward trend. Compared to the F9R0 configuration, the F9R9 design resulted in a reduction of 22.73 %–53.40 % in PSD and QSDV, reflecting enhanced sediment discharge capacity under reversed-flow-enhanced shear conditions. For configurations with the same unit layout, increasing the channel width led to a rising trend in PSD but a declining trend in QSDV. When the width increased from 0.25 mm to 0.70 mm, PSD increased by 33.11 %–217.28 %, while QSDV decreased by 59.53 %–96.68 %. This difference in variation ranges between PSD and QSDV is mainly due to QSDV being normalised by volume. This indicates that although wider channels may trap more sediment in relative terms, the absolute volume of deposition per unit volume is substantially reduced,

suggesting more efficient sediment transport. similarly, increasing the channel depth caused both PSD and QSDV to decrease. When the depth increased from 0.25 mm to 0.70 mm, PSD and QSDV dropped by 1.54 %–61.41 % and 61.86 %–86.22 %, respectively. These results suggest that deeper flow paths favor enhanced flushing and reduce sediment accumulation, particularly in low-velocity zones.

### 3.6. Cascading pathways linking structural parameters, flow characteristics, and emitter performance

To elucidate how emitter structural design parameters regulate flow processes and thereby affect hydraulic performance and sediment discharge capacity, correlation heatmaps were constructed between structural parameters, flow variables, hydraulic performance indicators, and anti-clogging performance indicators (Fig. 8). The hydraulic performance indicators—flow index ( $y$ ) and flow coefficient ( $K$ )—exhibited significant correlations ( $P < 0.05$ ) with multiple structural parameters. For example, the flow index showed strong associations with channel width, volume, mean velocity, hydraulic diameter, number of forward-flow units, and channel depth. Similarly, the anti-clogging indicators—percentage of sediment deposition (PSD) and quantity of sediment deposited per unit volume (QSDV)—also demonstrated significant correlations ( $P < 0.05$ ) with several structural variables, most notably mean velocity, hydraulic diameter, number of forward-flow units, and channel depth.

To further quantify the relative contributions of different structural parameters to performance outcomes, SHAP (Shapley Additive

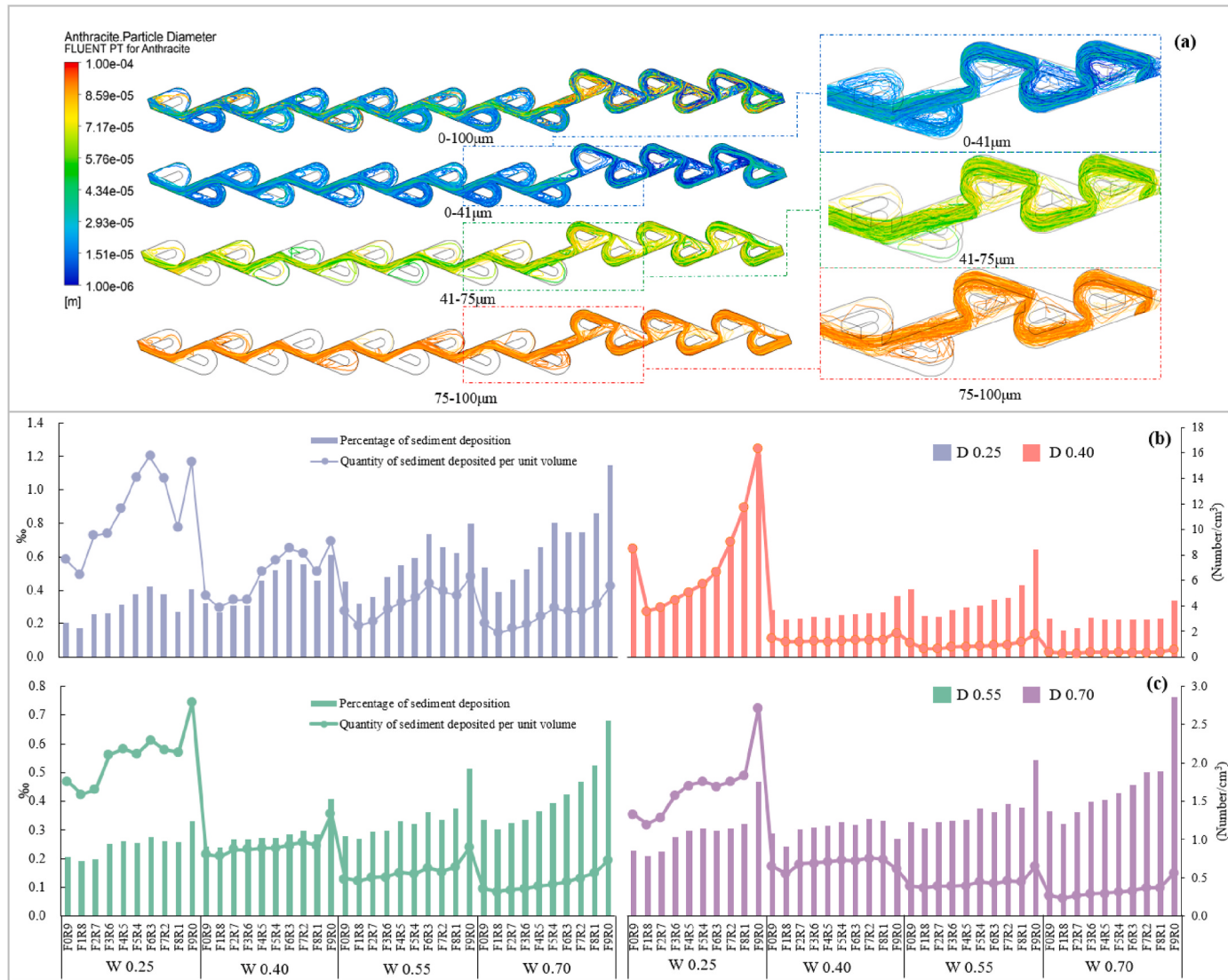


**Fig. 7.** Effects of structural parameters of the novel flow path configuration on sediment discharge performance. (a) Migration behavior of sediment particles with varying diameters inside the emitter flow path, illustrating differences in transport trajectories, settling tendencies, and potential clogging locations. (b) Variations in the percentage of sediment deposition (PSD) and the quantity of sediment deposited per unit volume (QSDV) for flow path depths of 0.25 mm and 0.40 mm under different structural configurations, showing how geometry influences deposition under shallower channels. (c) Variations in PSD and QSDV for flow path depths of 0.55 mm and 0.70 mm under different structural configurations, highlighting performance trends in deeper channels. Note: W and D denote the flow path width and depth, respectively, both of which critically affect particle-flow interactions and anti-clogging capacity.

Explanations) analysis was applied (Fig. 9). For hydraulic performance, the most influential parameters were hydraulic diameter (SHAP = 95.11), number of forward-flow units (39.00), channel depth (36.73), and width-to-depth ratio (W/D) (39.00). For anti-clogging performance, the influence weights were more pronounced, ranking as hydraulic diameter (340.86), number of forward-flow units (138.21), channel depth (131.63), and W/D (125.13).

The integrated mechanism pathway (Fig. 10) illustrates how key structural parameters indirectly influence emitter hydraulic and sediment discharge performance by modulating hydrodynamic variables such as mean velocity and turbulent kinetic energy (TKE). For the flow index, mean velocity emerged as the most critical hydrodynamic determinant, whereas TKE had the greatest impact on PSD. The analysis highlights that hydraulic diameter and the number of forward-flow units are the core structural variables governing system performance, with velocity being the primary hydrodynamic driver. Based on the fuzzy comprehensive evaluation method, all 160 treatments were assessed (detailed procedure in the Supplementary Materials). The results

(Fig. 11) indicated that the highest evaluation score was achieved under the configuration of channel depth = 0.40 mm, channel width = 0.25 mm, and forward-flow to reverse-flow unit ratio of F9R0.

#### 4. Discussion

This study constructed a multi-layered coupling framework linking structural parameters, flow characteristics, and performance responses, providing a systematic understanding of how geometric configurations of emitter flow paths regulate hydraulic efficiency and anti-clogging performance. Correlation and SHAP-based attribution analyses identified hydraulic diameter, number of forward-flow units, channel depth, and width-to-depth ratio (W/D) as the most influential parameters affecting key performance indicators, including the flow index, flow coefficient, sediment deposition and discharge ratio ( $\phi$ ), and the quantity of sediment deposited per unit volume (QSDV). Among these, hydraulic diameter had the highest impact on sediment discharge performance (SHAP = 340.86), followed by the number of forward units

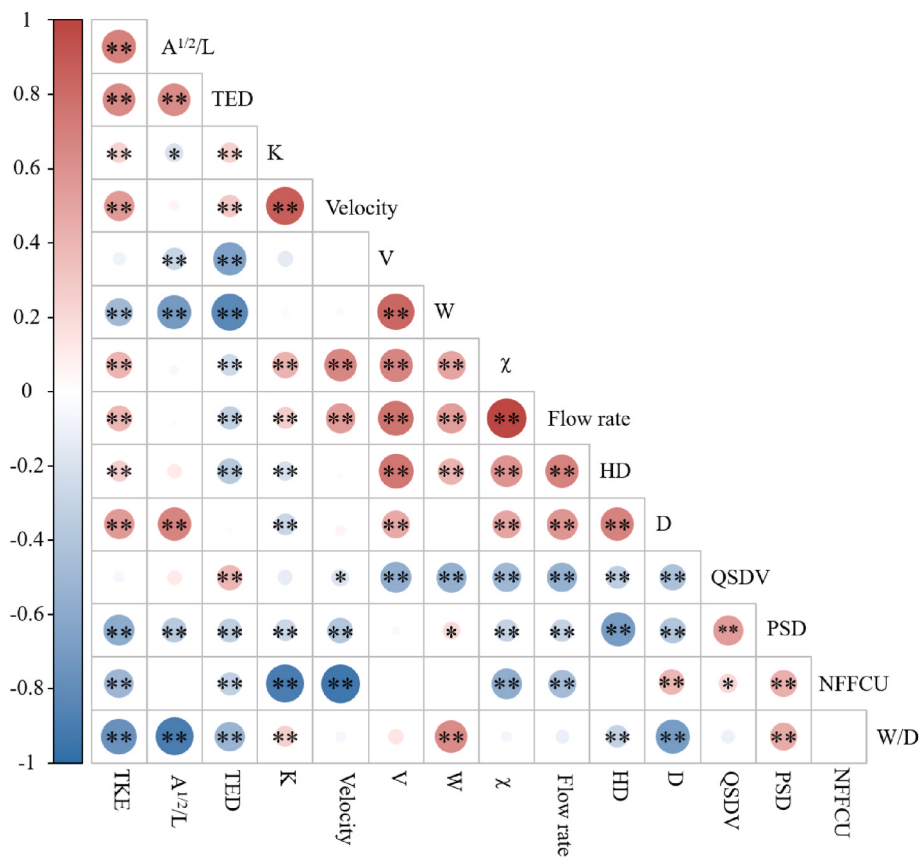


**Fig. 8.** Correlation heatmap among emitter structural parameters, flow parameters, hydraulic performance, and sediment discharge performance; Note: W: width; D: depth; L: length; HD: hydraulic diameter; NFFCU: number of forward flow channel units; V: volume;  $\chi$ : flow index K: flow coefficient; TKE: turbulence kinetic energy; TED: turbulence eddy dissipation;  $\varphi$ : sediment deposition and discharge ratio; QSDV: the quantity of sediment deposited per unit volume; PSD: the percentage of sediment deposition; HP: hydraulic performance; SDC: sediment discharge capacity. Asterisks indicate significance levels: \* $p < 0.05$ ; \*\* $p < 0.01$ .

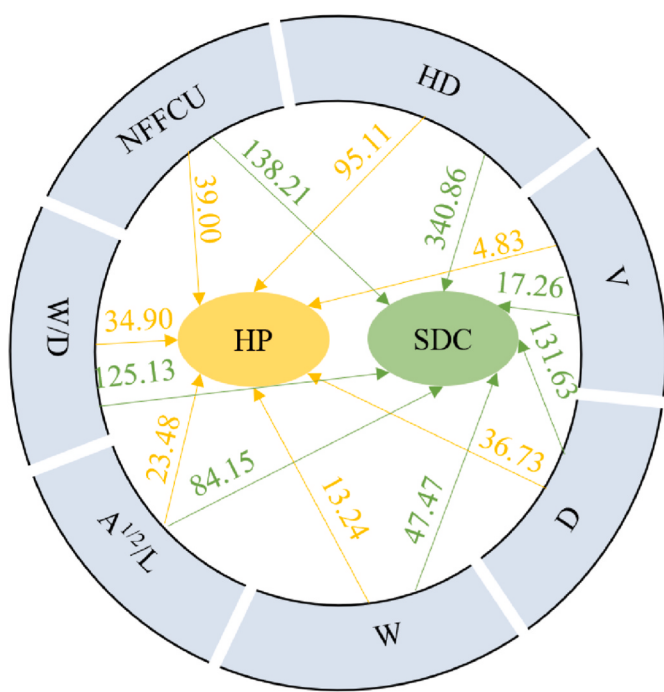


**Fig. 9.** Contribution pathways to emitter performance based on the SHAP (SHapley Additive exPlanations) method; Note: W: width; D: depth; L: length; HD: hydraulic diameter; NFFCU: number of forward flow channel units; V: volume; HP: hydraulic performance; SDC: sediment discharge capacity.

(138.21) and channel depth (131.63), indicating the dominant role of geometric scaling in regulating sediment migration mechanisms. Physically, an increase in hydraulic diameter alters the cross-sectional flow area, redistributes velocity gradients, and modulates the size and intensity of coherent turbulent structures (Liu et al., 2023; Xiao et al., 2020). A moderate enlargement enhances near-wall shear and sustains turbulent kinetic energy (TKE), which helps detach and transport sediment particles along the channel walls. Conversely, excessive enlargement reduces mean velocity and dissipates turbulence, allowing sediment to settle.

Similarly, the number of forward-flow units plays a critical role in shaping the internal disturbance field. A higher number of forward-flow units tends to maintain more stable unidirectional flow but suppresses vortex generation, reducing the flushing of particles from low-velocity regions (Zhang et al., 2025). In contrast, reducing forward-flow units and integrating reverse-disturbance elements strengthens shear layers, promotes localised recirculation, and redistributes TKE into stagnant zones—conditions that favor sediment resuspension and downstream transport (Gao & Stenstrom, 2018). Channel depth and W/D ratio further influence turbulence anisotropy and boundary layer development: shallow, wide channels accelerate lateral shear but may weaken vertical mixing, while deep, narrow channels intensify axial velocity but limit transverse turbulent exchange (Nguyen et al., 2016).

Three-dimensional distributions of turbulent dissipation and TKE under different structural configurations highlight the amplifying effects of geometric disturbances in critical regions such as bends, contractions, and cross-sectional transitions. This underscores the significance of micro-scale flow path design in fine-tuning local hydrodynamics. Based on the above mechanisms, the following design strategies are proposed

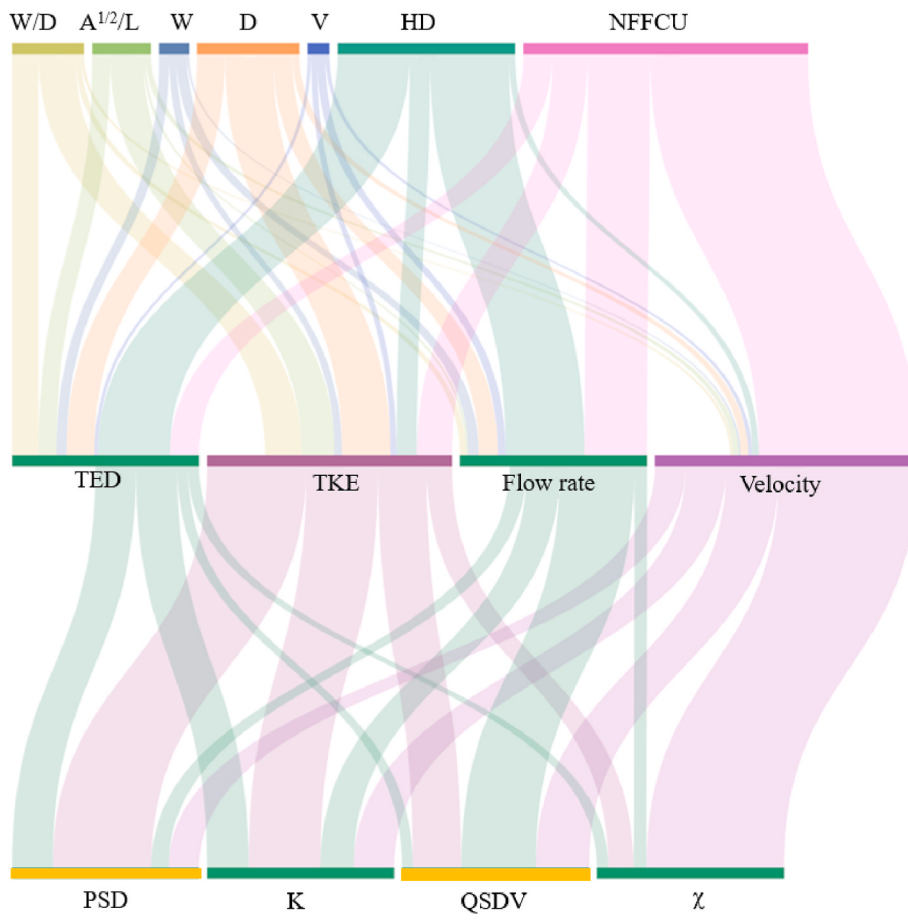


**Fig. 10.** Cascading effects from structural parameters to flow characteristics and final emitter performance. Note: W: width; D: depth; L: length; HD: hydraulic diameter; NFFCU: number of forward flow channel units; V: volume;  $\chi$ : flow index K: flow coefficient; TKE: turbulence kinetic energy; TED: turbulence eddy dissipation; QSDV: the quantity of sediment deposited per unit volume; PSD: the percentage of sediment deposition; Asterisks indicate significance levels: \* $p < 0.05$ ; \*\* $p < 0.01$ .

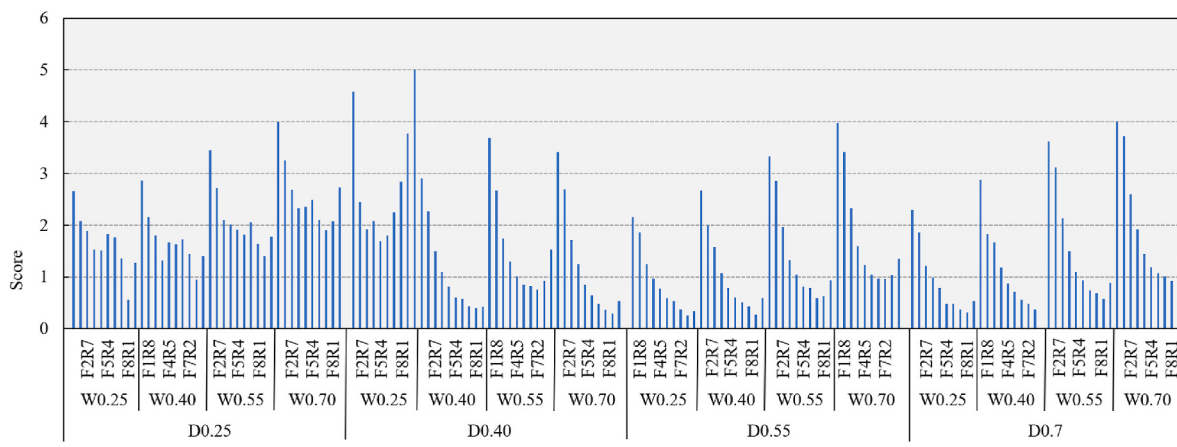


**Fig. 11.** Comprehensive evaluation scores for different treatments.

to enhance emitter performance: (1) Reduce forward-flow units and integrate reverse-disturbance elements to reinforce internal shear and vortex generation; (2) Optimise hydraulic diameter and W/D ratio according to sediment characteristics to avoid over-narrowing or excessive widening; (3) Adopt turbulence characteristics (TKE, eddy dissipation) as core control indicators, ensuring that channel geometry sustains energy levels needed for long-term anti-clogging performance. These insights establish a clear mechanism linking structural regulation,

turbulence restructuring, and performance response, and validate a disturbance-driven anti-clogging design pathway. Future research should integrate CFD-DEM coupling with multi-scale experimental validation to further clarify how sediment characteristics (e.g., size, shape, cohesion) interact with microchannel geometry, enabling adaptive emitter designs under complex water quality conditions.

## 5. Conclusions

This study developed a micro-scale Euler–Lagrange simulation framework to evaluate sediment transport dynamics and anti-clogging performance in drip irrigation emitters under high-sediment water conditions. The model, incorporating Discrete Phase Model (DPM) particle tracking and Rebound boundary conditions, demonstrated strong accuracy (error <10 %) in capturing sediment deposition and flow behaviour in confined microchannels. Results revealed that introducing reverse-flow disturbance units enhanced local shear and vortex intensity, increasing turbulent kinetic energy and resuspension capability. Under different forward- and reverse-flow unit configurations, PSD and QSDV both decreased by 22.73 %–53.40 %. SHAP-based contribution analysis identified hydraulic diameter, forward-flow unit count, and channel depth as dominant structural factors, with hydraulic diameter exerting the strongest influence by modulating local energy dissipation. A nonlinear “window effect” was observed, indicating threshold sensitivity in particle response to structural perturbations. These findings provide mechanistic insights and optimisation strategies for emitter design.

The present study was conducted under controlled CFD-simulation conditions using a single particle size distribution representative of Yellow River sediment, and did not consider multiple particle size distributions, biological sediment formation, or long-term operational durability. Although the RNG k–e turbulence model achieved good agreement with experimental validation in this study, its low-Reynolds-number limitations and potential differences under varying sediment types should be addressed in future research. Furthermore, field-scale tests under real irrigation conditions are needed to validate the model predictions, including performance against biological sediment, structural wear, and durability over extended operational periods. In addition, the evaluation of channel structural configurations in this study was based on a fuzzy comprehensive evaluation method, in which the weighting scheme was subjectively defined and thus inherently influenced by human judgment. This introduces a certain degree of subjectivity and limits the applicability of the evaluation results to the specific conditions and objectives of this study. Future work should also incorporate experimental visualisation and CFD–DEM coupling to better resolve particle–surface interactions, as well as integrate non-spherical particle shapes, surface roughness, and adhesive properties into the modelling framework to improve clogging prediction accuracy.

## CRediT authorship contribution statement

**Peng Hou:** Writing – review & editing, Writing – original draft, Methodology, Investigation, Conceptualization. **Tuo Yin:** Writing – review & editing, Methodology. **Shengqi Jian:** Project administration, Formal analysis, Data curation. **Yan Li:** Writing – review & editing. **Xinhao Gao:** Writing – review & editing. **Xueli Zhang:** Writing – review & editing, Methodology. **Changjian Ma:** Writing – review & editing, Investigation, Funding acquisition, Conceptualization.

## Data availability statement

Data will be made available on request.

## Declaration of competing interest

The authors declare that they have no known competing financial interests or personal relationships that could have appeared to influence the work reported in this paper.

## Acknowledgments

Funding support for this research was provided by National Natural Science Foundation of China (Grant No. 52409074), National Key

Research and Development Plan (2023YFD1902703), Key R&D and Promotion Special Project of Henan Province (252102321111), Key Scientific Research Project of Higher Education Institutions in Henan Province (25A570003), Technical System of Ecological Agriculture of Modern Agricultural Technology System in Shandong Province (SDAIT-30-01), and the Taishan Scholars Program (tstp20230646)

## Appendix A. Supplementary data

Supplementary data to this article can be found online at <https://doi.org/10.1016/j.biosystemseng.2025.104295>.

## References

- Abdorahimzadeh, S., Bölkükaya, Z., Vainio, S. J., Liimatainen, H., & Elbuken, C. (2024). Anomalous electrohydrodynamic cross-stream particle migration. *Physics of Fluids*, 36, Article 043609. <https://doi.org/10.1063/5.0200283>
- AL-Muhammad, J., AL-Muhammad, J., Tomas, S., Tomas, S., & Ait-Mouheb, N. (2018). Micro-PIV characterization of the flow in a milli-labyrinth-channel used in drip irrigation. *Experiments in Fluids*, 59(12), 181–191. <https://doi.org/10.1023/A:1024905302323>
- Boutsikakis, A., Fede, P., & Simonin, O. (2022). Effect of electrostatic forces on the dispersion of like-charged solid particles transported by homogeneous isotropic turbulence. *Journal of Fluid Mechanics*, 938, A33. <https://doi.org/10.1017/jfm.2022.189>
- Cha, H. T., Fallahi, H., Dai, Y. C., Yuan, D., An, H. J., Nguyen, N. T., & Zhang, J. (2022). Multiphysics microfluidics for cell manipulation and separation: A review. *Lab on a Chip*, 22(3), 423–444. <https://doi.org/10.1039/DLCO00869B>
- Ching, E. J., Brill, S. R., Barnhardt, M., & Ihme, M. (2020). A two-way coupled euler–lagrange method for simulating multiphase flows with discontinuous galerkin schemes on arbitrary curved elements. *Journal of Computational Physics*, 405, Article 109096. <https://doi.org/10.1016/j.jcp.2019.109096>
- Dallagi, H., Ait-Mouheb, N., Soric, A., & Boiron, O. (2024). Simulation of the flow characteristics of a labyrinth milli-channel used in drip irrigation. *Biosystems Engineering*, 239, 114–129. <https://doi.org/10.1016/j.biosystemseng.2024.02.004>
- De Marchis, M., Bruno, F., Saccone, D., & Napoli, E. (2025). Performance of emitters in drip irrigation systems using computational fluid dynamic analysis. *Water*, 17, 689. <https://doi.org/10.3390/w17050689>
- De Marchis, M., & Milici, B. (2016). Turbulence modulation by micro-particles in smooth and rough channels. *Physics of Fluids*, 28, Article 115101. <https://doi.org/10.1063/1.4966647>
- Felix, T., Espen-Alexander-F, I., Lars, A., & Inga, S. (2025). Explaining human activity recognition with SHAP: Validating insights with perturbation and quantitative measures. *Computers in Biology and Medicine*, 188, Article 109838. <https://doi.org/10.1016/j.combiomed.2025.109838>
- Feng, J., Li, Y., Wang, W., & Xue, S. (2018). Effect of optimization forms of flow path on emitter hydraulic and anti-clogging performance in drip irrigation system. *Irrigation Science*, 36(1), Article 37e47. <https://doi.org/10.1007/s00271-017-0561-9>
- Gao, H. W., & Stenstrom, M. K. (2018). Evaluation of three turbulence models in predicting the steady state hydrodynamics of a secondary sedimentation tank. *Water Research*, 143, 445–456. <https://doi.org/10.1016/j.watres.2018.06.067>
- Guo, B., Xiao, Y. X., Rai, A. K., Liang, Q. W., & Liu, J. (2021). Analysis of the air-water-sediment flow behaviour in pelton buckets using an eulerian-lagrangian approach. *Energy*, 218, Article 119522. <https://doi.org/10.1016/j.energy.2020.119522>
- Hancock, J. T., Khoshgoftaar, T. M., & Liang, Q. X. (2025). A problem-agnostic approach to feature selection and analysis using SHAP. *Journal of Big Data*, 12(1), 1–22. <https://doi.org/10.1186/s40537-024-01041-1>
- Hou, P., Liu, L., Muhammad, T., Li, Y., Wang, X., Shi, N., Xiao, Y., Ma, C., & Li, Y. (2024). Effect of fertilization on emitter clogging in drip irrigation using high sediment water: Perspective of sediment discharge capacity. *Agricultural Water Management*, 294, Article 108723. <https://doi.org/10.1016/j.agwat.2024.108723>
- Hou, P., Puig-Bargués, J., Liu, L., Xiao, Y., Zhou, B., & Li, Y. K. (2024). New anti-clogging perspective by discharging sediment from drip irrigation emitters with high-sediment loaded water. *Irrigation Science*, 42, 645–656. <https://doi.org/10.1007/s00271-023-00884-5>
- Hua, G., Salo, M. W., Schmit, C. G. H., & Hay, C. H. (2016). Nitrate and phosphate removal from agricultural subsurface drainage using laboratory woodchip bioreactors and recycled steel byproduct filters. *Water Research*, 102, 180–189. <https://doi.org/10.1016/j.watres.2016.06.022>
- Khalidi, N., Chouari, Y., Mhiri, H., & Bournot, P. (2016). Pulsation effects on pollutant and sediment transport in free-surface flow. *Environmental Pollution*, 219, 685–695. <https://doi.org/10.1016/j.envpol.2016.06.070>
- Kovalchuk, N. M., & Simmons, M. J. H. (2023). Review of the role of surfactant dynamics in drop microfluidics. *Advances in Colloid and Interface Science*, 312, Article 102844. <https://doi.org/10.1016/j.cis.2023.102844>
- Li, Y. F., Feng, X. Y., Han, X. C., Sun, Y. T., & Li, H. (2024). Analysis of anti-clogging performance and particle transport characteristics of a stellate irrigation emitter. *Biosystems Engineering*, 242, 50–66. <https://doi.org/10.1016/j.biosystemseng.2024.04.010>
- Li, Y. F., Feng, X. Y., Han, X. C., Sun, Y. T., Liu, Y. D., Yao, M., Liu, H. Y., & He, Q. H. (2023). Analysis of internal flow characteristics and determination of the core

- structural parameters of a stellate labyrinth channel irrigation emitter. *Biosystems Engineering*, 231, 1–19. <https://doi.org/10.1016/j.biosystemseng.2023.05.006>
- Li, Y., Feng, J., Xue, S., Muhammad, T., Chen, X., & Wu, N. (2019). Formation mechanism for emitter composite clogging in drip irrigation system. *Irrigation Science*, 37(2), 169–181. <https://doi.org/10.1007/s00271-018-0612-x>
- Liu, Z., Shao, W. Q., Sun, Y., & Sun, B. H. (2022). Scaling law of the one-direction flow characteristics of symmetric tesla valve. *Engineering applications of computational fluid mechanics*, 16(1), 441–452. <https://doi.org/10.1080/19942060.2021.2023648>
- Liu, S. J., Zhang, C. Q., Shen, T., Zhan, Z. D., Peng, J., Yu, C. L., Jiang, L., & Dong, Z. C. (2023). Efficient agricultural drip irrigation inspired by fig leaf morphology. *Nature Communications*, 14, 5934. <https://doi.org/10.1038/s41467-023-41673-0>
- Nguyen, A. V., An-Vo, D. A., Tran-Cong, T., & Evans, G. M. (2016). A review of stochastic description of the turbulence effect on bubble-particle interactions in flotation. *International Journal of Mineral Processing*, 156, 75–86. <https://doi.org/10.1016/j.minpro.2016.05.002>
- Pietrzik, K., Horwitz, J. A. K., Najjar, F. M., & Minich, R. W. (2022). On analysis and stochastic modelling of the particle kinetic energy equation in particle-laden isotropic turbulent flows. *Physics of Fluids*, 34(1), Article 013316. <https://doi.org/10.1063/5.0075650>
- Puertes, C., Bautista, I., Lidón, A., & Frances, F. (2021). Best management practices scenario analysis to reduce agricultural nitrogen loads and sediment yield to the semiarid Mar Menor coastal lagoon (spain). *Agricultural Systems*, 188, Article 103029. <https://doi.org/10.1016/j.agsy.2020.103029>
- Shen, Y., Puig-Bargues, J., Li, M. Y., Xiao, Y., Li, Q., & Li, Y. K. (2022). Physical, chemical and biological emitter clogging behaviours in drip irrigation systems using high-sediment loaded water. *Agricultural Water Management*, 270, Article 107738. <https://doi.org/10.1016/j.agwat.2022.107738>
- Shi, H. H., Nie, K. X., Dong, B., Long, M. Q., Xu, H., & Liu, Z. C. (2019). Recent progress of microfluidic reactors for biomedical applications. *Chemical Engineering Journal*, 361, 635–650. <https://doi.org/10.1016/j.cej.2018.12.104>
- Shrestha, S., Kulandaivelu, J., Sharma, K., Jiang, G., & Yuan, Z. (2020). Effects of dosing iron and alum-containing waterworks sludge on sulfide and phosphate removal in a pilot sewer. *Chemical Engineering Journal*, 387, Article 124073. <https://doi.org/10.1016/j.cej.2020.124073>
- Song, P., Feng, G., Brooks, J., Zhou, B., Zhou, H., Zhao, Z., & Li, Y. (2019). Environmental risk of chlorine-controlled clogging in drip irrigation system using reclaimed water: The perspective of soil health. *Journal of Cleaner Production*, 232, 1452–1464. <https://doi.org/10.1016/j.jclepro.2019.06.050>
- Song, J., Wei, Y., Sun, G., & Chen, J. (2017). Experimental and CFD study of particle deposition on the outer surface of vortex finder of a cyclone separator. *Chemical Engineering Journal*, 309, 249–262. <https://doi.org/10.1016/j.cej.2016.10.019>
- Sun, Z., Liang, L., Liu, C., Zhu, Y., Zhang, L., & Yang, G. (2021). CFD simulation and performance optimization of a new horizontal turbo air classifier. *Advanced Powder Technology*, 32, 977–986. <https://doi.org/10.1016/j.apt.2021.01.041>
- Tong, X. Y., Wu, P. T., Liu, X. F., & Zhang, L. (2025). Hydraulic analysis and design of subsurface irrigation system with ceramic emitters based on iterative method: An exploration in north China. *Computers and Electronics in Agriculture*, 229, Article 109918. <https://doi.org/10.1016/j.compag.2025.109918>
- Wang, C. C., & Wu, R. M. (2018). Experimental and simulation of a novel hydrocyclone-tubular membrane as overflow pipe. *Separation and Purification Technology*, 198, 60–67. <https://doi.org/10.1016/j.seppur.2017.04.034>
- Wu, D., Li, Y., Liu, H., Yang, P., Sun, H., & Liu, Y. (2013). Simulation of the flow characteristics of a drip irrigation emitter with large eddy methods. *Mathematical and Computer Modelling*, 58(3e4), Article 497e506. <https://doi.org/10.1016/j.mcm.2011.10.074>
- Xiao, Y., Liu, Y., Ma, C., Muhammad, T., Zhou, B., Zhou, Y., Song, P., & Li, Y. K. (2021). Using electromagnetic fields to inhibit biofouling and scaling in biogas slurry drip irrigation emitters. *Journal of Hazardous Materials*, 401, Article 123265. <https://doi.org/10.1016/j.jhazmat.2020.123265>
- Xiao, Y., Sawicka, B., Liu, Y. Z., Zhou, B., Hou, P., & Li, Y. K. (2020). Visualizing the macroscale spatial distributions of biofilms in complex flow channels using industrial computed tomography. *Biofouling*, 36(2), 115–125. <https://doi.org/10.1080/08927014.2020.1728260>
- Xu, Z. C., Chen, X. Z., Liu, J. G., Zhang, Y., Chau, S., Bhattacharai, N., Wang, Y., Li, Y. J., Thomas-Connor, T., & Li, Y. K. (2020). Impacts of irrigated agriculture on food-energy-water-CO<sub>2</sub> nexus across metacoupled systems. *Nature Communications*, 11, 5837. <https://doi.org/10.1038/s41467-020-19520-3>
- Yang, C. L., Guan, X. F., Xu, Q. Y., Xing, W. R., Chen, X. Y., Chen, J. G., & Jia, P. (2024). How can SHAP (SHapley additive exPlanations) interpretations improve deep learning-based urban cellular automata model? *Computers, Environment and Urban Systems*, 111, Article 102133. <https://doi.org/10.1016/j.compenvurbsys.2024.102133>
- Yang, B., Wang, F. X., Wang, J. D., Wang, C. J., & Qiu, X. F. (2024). Numerical simulation and optimization of the inlet structure of dentiform emitters in drip-irrigation systems. *Biosystems Engineering*, 246, 183–190. <https://doi.org/10.1016/j.biosystemseng.2024.08.004>
- Yang, X. L., Xi, T., Qin, Y. B., Zhang, H., & Wang, Y. W. (2024). Computational fluid dynamics-discrete phase method simulations in process engineering: A review of recent progress. *Applied Sciences*, 14(9). <https://doi.org/10.3390/app14093856>
- Zhang, K., Li, N., Fu, S. H., Mu, H. L., & Lu, B. J. (2025). The mechanism of surface cover influences the sediment transport capacity. *Journal of Hydrology*, 651, Article 132527. <https://doi.org/10.1016/j.jhydrol.2024.132527>
- Zhang, Z., Lu, J., Zhang, Z., Yang, J., Xin, K., Zhao, Z., An, L., & Kong, D. (2022). Effect of potassium ferrate treatment on adhesive gelatinous biopolymer structure and erosion resistance of sewer sediments: Promotion or inhibition? *Chemical Engineering Journal*, 431, Article 134025. <https://doi.org/10.1016/j.cej.2021.134025>
- Zhang, W. Q., Lv, C., Zhao, X., Dong, A. H., & Niu, W. Q. (2021). The influence mechanism of the main suspended particles of yellow river sand on the emitter clogging-An attempt to improve the irrigation water utilization efficiency in yellow river basin. *Agricultural Water Management*, 258, Article 107202. <https://doi.org/10.1016/j.agwat.2021.107202>
- Zhou, B., Hou, P., Xiao, Y., Song, P., Xie, E., & Li, Y. K. (2021). Visualizing, quantifying, and controlling local hydrodynamic effects on biofilm accumulation in complex flow paths. *Journal of Hazardous Materials*, 416, Article 125937. <https://doi.org/10.1016/j.jhazmat.2021.125937>
- Zhou, H. X., Li, Y. K., Wang, Y., Zhou, B., & Bhattacharai, R. (2019). Composite fouling of drip emitters applying surface water with high sand concentration: Dynamic variation and formation mechanism. *Agricultural Water Management*, 215, 25–43. <https://doi.org/10.1016/j.agwat.2019.01.009>
- Zhou, W., Zhang, L., Wu, P., Cai, Y., Zhao, X., & Yao, C. (2020). Hydraulic performance and parameter optimisation of a microporous ceramic emitter using computational fluid dynamics, artificial neural network and multi-objective genetic algorithm. *Biosystems Engineering*, 189, 11e23. <https://doi.org/10.1016/j.biosystemseng.2019.11.006>